Scientific Reports

https://doi.org/10.1038/s41598-026-46438-5

Article in Press

Iron-modified biochar enhanced the activation of peracetic acid for removal of imidacloprid: efficiency, active species and catalytic mechanism

Received: 16 December 2025

Accepted: 25 March 2026

Published online: 03 April 2026

Cite this article as: He J., Wang B., Sun H. *et al.* Iron-modified biochar enhanced the activation of peracetic acid for removal of imidacloprid: efficiency, active species and catalytic mechanism. *Sci Rep* (2026). https://doi.org/10.1038/s41598-026-46438-5

Jinjin He, Baoyan Wang, Hongwei Sun, Yucan Liu, Gang Wang, Xiaoyong Yang & Yanxiang Zhang

Iron-modified biochar enhanced the activation of peracetic acid for removal of imidacloprid: Efficiency, active species and catalytic mechanism

Jinjin He[a], Baoyan Wang[b], Hongwei Sun[a*], Yucan Liu[b], Gang Wang[a], Xiaoyong Yang[a], Yanxiang Zhang[a*]

[a] *School of Environmental and Materials Engineering, Yantai University, Yantai 264005, China*

[b] *School of Civil Engineering, Yantai University, Yantai 264005, China*

Corresponding author:

E−mail: 12821306@qq.com (Hongwei Sun); 15092166641@163.com; yanxiangzhang@ytu.edu.cn (Yanxiang Zhang)

Abstract

Imidacloprid (IMI) is a highly toxic organic pollutant. Therefore, effective IMI treatment methods must be developed. This study synthesized iron-modified rape straw biochar (Fe-RSB) to activate peracetic acid (PAA) for IMI removal from water. At the optimal concentrations of 0.55 g•L^{-1} for Fe-RSB and 0.25 mM for PAA, the removal of IMI reached 81.6% after 60 min. Additionally, the IMI removal was minimally affected over a broad pH range (3-11). $CH_3C(O)O\cdot$ and $CH_3C(O)OO\cdot$ played crucial roles in the IMI degradation. The degradation pathway of IMI consisted of three pathways, and the ecological hazards of most intermediates were lower than those of IMI. The effect of Cl^- on IMI removal was concentration dependent, 2 mM Cl^- showed slight inhibition, while 10 mM Cl^- promoted the degradation. In contrast, both HA and HCO_3^- exhibited inhibitory effects across the tested concentration ranges. After five cycles, the removal of IMI reached 61.9%, indicating the stability of Fe-RSB. Overall, a new Fe-RSB/PAA process is proposed for the degradation of IMI.

Keywords: Advanced oxidation processes, Imidacloprid, Iron-modified biochar, Peracetic acid, Mechanism

1. Introduction

Due to the constant pursuit of high-quality and high-efficiency development of agricultural products, large amounts of pesticides have been spread on croplands and enter water and soil ecosystems every year [1,2]. Imidacloprid (IMI) is a neonicotinoid insecticide frequently used in agriculture [3,4]. However, a small percentage of IMI adsorbed onto crops can be transferred to water through rainfall or other means (less than 1%) [5]. In addition, the excellent stability and high water solubility (0.51 g•L^{-1} 20 °C) of IMI enable it to resist natural self-degradation [6]. It is frequently detected in water, such as the Yangtze and Turkish rivers [7,8]. Researchers have found that IMI not only exerts significant toxicity on non-target aquatic invertebrates but also poses risks to the liver of mammals and humans, thereby disrupting the ecological balance [9,10]. Therefore, continuous accumulation of IMI may cause toxicity and impair ecosystem functions [11]. Hence, the search for effective methods to degrade IMI has continuously been a subject of considerable attention.

In advanced oxidation processes (AOPs), oxidants are employed to generate free radicals that destroy or mineralize pollutants. [12]. It has significant potential for degrading organic pollutants in wastewater [13,14]. The selection of oxidants is a crucial factor for

ensuring the efficient removal of pollutants. Peracetic acid (PAA) is a safe oxidant that is widely used for disinfection and oxidation in various industries (e.g., medicine and health, food processing, and textile manufacturing) [15]. It has many advantages such as a high redox potential range from 1.06 V (under alkaline conditions) to 1.96 V (under acidic conditions), low toxicity, and minimal by-product generation [16]. Therefore, PAA-based advanced oxidation processes have been extensively applied for the removal of various hazardous substances from wastewater [17,18]. For example, the removal of pharmaceuticals, hexabromocyclododecane, and acids with organic compounds was achieved by UV/PAA, ultrasound/PAA, and cobalt/PAA processes, respectively [19-21]. However, the catalysts for activating PAA in these systems are energy-costly and may lead to secondary pollution. Therefore, there is a need to develop a nontoxic, environmentally friendly, and stable green catalyst to activate PAA and achieve environmental and nonhazardous goals.

Biochar is a green catalyst that is widely applied in soil and water decontamination because of its simple preparation process, low cost, large surface area, and abundant functional groups [22,23]. Therefore, the use of biochar to activate PAA demonstrates high potential for removing harmful substances and realizing the recycling of various biowastes [24]. For instance, wheat straw biochar/PAA removed 30.5%

of Acid Orange [25], and the SBC/PAA system degraded 65% of SMX within 30 min. However, unmodified biochar performs poorly in the activation of PAA [26]. Therefore, further modification of the physicochemical properties of biochar is urgently required to obtain higher catalytic efficiency.

The modification method of doping transition metals (e.g., Mn, Fe, and Co) into biochar not only prevents metal leakage but also increases the number of active sites [27,28]. Among the transition metals, iron is considered an ideal and effective modifier that can enhance the activation performance of biochar for PAA. Iron possesses excellent characteristics such as stable physical properties, low toxicity, and high conductivity [29,30]. Therefore, the use of Fe-doped biochar to activate PAA has gained widespread attention. For instance, the Fe-biochar/PAA system achieved 99.9% removal of Acid Orange, $CoFe_2O_4$-biochar/PAA removed 96% of TCH, and the Fe-SBC/PAA process degraded 92% of SMX, which was 27% higher than that of the SBC/PAA process [31]. While iron-modified biochars have been widely studied for activating various oxidants, their application in PAA activation for IMI removal remains unexplored. More importantly, most reported iron-modified biochars require complex synthesis procedures or exhibit limited catalytic efficiency due to poor iron dispersion. In contrast, our Fe-RSB was

synthesized via a simple one-step pyrolysis method that ensures uniform distribution of iron species on the biochar matrix. Compared to previously reported iron-modified biochars (e.g., Fe-SBC, Fe-WB), Fe-RSB demonstrates superior PAA activation performance, achieving 81.6% IMI removal within 60 min—significantly higher than the 48.2% removal achieved by unmodified RSB/PAA system. This enhanced performance is attributed to: (i) the synergistic effect between iron species and oxygen-containing functional groups (–OH, C=O, C–O) on the biochar surface; (ii) the mesoporous structure (pore size ~9 nm) that facilitates mass transfer; and (iii) the efficient Fe^{3+}/Fe^{2+} redox cycling that sustains radical generation.

The objectives are threefold: (I) to evaluate the impacts of PAA concentration, Fe-RSB dosage, and pH on IMI degradation kinetics; (II) to elucidate the activation mechanism using quenching tests and spectroscopic techniques (e.g., XPS, XRD); and (III) to identify degradation intermediates and pathways while quantifying toxicity changes. This work offers both a viable approach for IMI remediation and an advancement in the fundamental science of biochar-enhanced advanced oxidation.

2.Materials and methods

2.1 Chemicals

IMI was obtained from Macklin Biochemical Technology Co., Ltd.

(Shanghai, China). The PAA disinfectant solution was obtained from Aladdin Biochemical Technology Co., Ltd. (Shanghai, China). The details of the chemical reagents used in the experiments are in supplementary material. All solutions used in the experiments were prepared with ultrapure water.

Rape straw from farmland (Nanjing, China) was used as the raw material for biochar. The raw material was washed with deionized water to remove impurities and then dried in an oven (80 ℃). It was then grounded through a sieve (100 mesh) to obtain rape straw powder (RS), which was stored for future use.

2.2 Preparation of biochar

Fe-RSB was prepared under optimal conditions (Fe^{3+}/RS mass ratio of 2:1, pyrolysis at 400 °C) based on preliminary optimization experiments (Table S4), which showed that these parameters maximized IMI removal efficiency. Briefly, 2 g of RS was mixed with $FeCl_3 \cdot 6H_2O$ (6.65 g) in deionized water (200 mL) with the Fe^{3+}/RS mass ratio of 2:1. After thorough mixing, the solution was stirred magnetically for 12 h at 25 ± 0.5 ℃. The filtered precipitates were dried in an oven (80 °C) for 3 h to obtain Fe-RS. Fe-RS was pyrolyzed in a tubular furnace (400 °C) under a continuous N_2 flow for 2 h to produce Fe-RSB, which was subsequently washed and dried at 80 ℃. The original RSB were obtained by repeating this procedure.

2.3 Experimental procedures

All experiments were conducted in conical flasks (200 mL). The sample was stirred on a constant temperature water bath shaker at a speed of 180 r/min. PAA (0.25 mM) and Fe-RSB (0.55 g•L^{-1}) were added to the IMI solution (10 mg/L, 100 mL). The samples were collected at the designated time and immediately quenched with excess $Na_2S_2O_3$ solution, followed by filtration through 0.22 μm organic filter membrane. Furthermore, the effect of reaction conditions on the IMI degradation were examined by adjusting the initial pH (3-11) of IMI solution with 0.1 mol•L^{-1} NaOH or HCl solution, Cl^- solution (0-10 mM), HCO_3^- solution (0-2 mM), and HA solution (0-10 mg/L). To test reusability, Fe-RSB was recycled, rinsed five times with deionized water, and dried under vacuum at 55 °C for the next cycle of the experiment. The experiments were repeated multiple times to reduce errors and enhance the reliability of the results.

The degradation kinetics of IMI were calculated using a pseudo-first-order (PFO) kinetic model (Eqs. 1).

$$\ln C_0/C_t = - k_{obs}t \quad (1)$$

Where k_{obs} (min^{-1}) is the rate constants, C_t (mg/L) is the concentration of IMI after reaction time t (min), and C_0 (mg/L) is the initial concentration of IMI.

2.4 Analytical methods

The PAA concentration was determined using the iodometric and potassium permanganate titration methods (see supplementary material). The characterization methods of RSB and Fe-RSB is in the supplementary material. The IMI concentration was assessed using UPLC-ESI-MS/MS (see supplementary material). ECOSAR software was used to investigate the impact of IMI and its by-products on the ecological environment.

3. Results and discussion

3.1 Biochar characterizations

The morphological structure of RSB and Fe-RSB was compared through SEM. Both the materials exhibited porous structures. The surface of RSB displayed a flat structure (**Error! Reference source not found.**a), but the surface of Fe-RSB displayed glossy particles (Fig. 1b), which are suggestive of iron-containing species. The successful loading of iron was further confirmed by EDS (Figure S1), and the increased specific surface area (from 8.01 to 17.39 m^2/g), collectively indicating that iron was effectively incorporated into the biochar matrix. Furthermore, the surface of used Fe-RSB also exhibited glossy particles (**Error! Reference source not found.**c, Figure S1). These results indicated that Fe^{3+} was successfully loaded onto RSB, which could increase the number of reactive sites [31]. The

N_2 adsorption-desorption isotherms of RSB and Fe-RSB were both Type IV isotherms with distinct hysteresis loops (**Error! Reference source not found.**d). The pore size distributions of the catalysts were predominantly centered at approximately 15 nm (**Error! Reference source not found.**e), indicating the formation of mesoporous structures (2 nm < d < 50 nm) [32]. The pore characterization parameters indicated that the specific surface area and pore volume of Fe-RSB were larger than those of RSB (see supplementary materials), providing more reactive sites and enhancing the contact area with PAA [33].

Functional groups are crucial active sites [34]. FTIR is often employed to monitor the functional groups of catalysts (**Error! Reference source not found.**f). The peaks of 3383-3495 cm^{-1}, 1624 cm^{-1}, 1384 cm^{-1}, 1141 cm^{-1} and 794 cm^{-1} in RSB were respectively attributed to −OH, C=C, C=O, C−O and C−H [35]. In contrast to RSB, it was observed that Fe-RSB exhibited a relatively small absorption band at 541 cm^{-1}, which could be due to the stretching vibration of Fe−O [36]. The positions of −OH stretching, aromatic C=O, C−O group, and Fe−O group shifted in the FTIR spectra of Fe-RSB. These results suggested that –OH, C=O, C−O, and Fe−O could provide reactive sites for activating PAA [37].

XPS was used to examine the chemical compositions and valence

state changes of RSB and Fe-RSB. Fe-RSB exhibited a new characteristic peak (Fe 2p) at a binding energy of 711 eV (**Error! Reference source not found.**a). The O 1s spectrum of RSB included two peaks: C−O (532.8 eV) and C=O (531.4 eV) (**Error! Reference source not found.**b). In the O 1s spectrum of Fe-RSB, the peaks of C−O and C=O were weakened, which indicated a change in the valence state of O 1s. Additionally, a new peak of Fe−O was appeared at a binding energy of 530.7 eV. The C 1s spectrum of RSB contained four peaks: C−C/C=C (284.8 eV), C−O (285.9 eV), C=O (288.8 eV), and O−C=O (293.4 eV) (**Error! Reference source not found.**c). However, the O−C=O peak disappeared in the C 1s spectrum of Fe-RSB. This could be attributed to the influence of Fe on the transformation of C−corresponding bonds, resulting in the conversion of the O−C=O to C−C/C=C [38]. Thus, it was confirmed that iron was successfully loaded onto the RSB.

3.2 Degradation of IMI in the different systems

IMI removal was tested using different systems (**Error! Reference source not found.**a). After 60 min of reaction, the removal efficiencies of RSB and Fe-RSB were 13.5% and 15.4%, respectively. This could be attributed to the adsorption of IMI by the catalysts. The degradation rate of IMI was 39.3% with PAA alone, indicating that PAA alone generated active radicals. When RSB and

Fe-RSB were separately added to the PAA solution, the removal efficiencies of IMI were 48.2% and 81.6%, with kobs of 0.0276 and 0.1066 min^{-1}, respectively, suggesting that the Fe-RSB/PAA process exhibited a higher degradation rate. Because the PAA solution contained H_2O_2, the impact of H_2O_2 on the IMI degradation was studied. The removal of IMI was relatively poor (35.3%), indicating that the Fe-RSB/H_2O_2 process had an insignificant impact on IMI degradation. The results might be because PAA had a lower energy (-0.25 eV) compared to H_2O_2 (0.57 eV) [39]. Overall, Fe-RSB effectively activated PAA to remove IMI (Eqs.2-5) [40].

$$Fe^{3+} + H_2O_2 \rightarrow Fe^{2+} + HO_2\bullet + H^+ \quad (2)$$

$$CH_3C(O)OOH + Fe^{3+} + H_2O \rightarrow CH_3C(O)OO\bullet + Fe^{2+} + H_3O^+ \quad (3)$$

$$CH_3C(O)OOH + Fe^{2+} \rightarrow CH_3C(O)O\bullet + Fe^{3+} + OH^- \quad (4)$$

$$CH_3C(O)OOH + Fe^{2+} \rightarrow CH_3C(O)O^- + Fe^{3+} + \bullet OH \quad (5)$$

3.3 Influence of various factors on the IMI degradation

3.3.1 Influence of Fe-RSB concentration

Error! Reference source not found.b illustrates the influence of Fe-RSB concentration on IMI degradation. As the Fe-RSB dosage

rose from 0.1 g•L^{-1} to 0.55 g•L^{-1}, the removal of IMI rose from 31.8% to 81.6%, owing to the fact that sufficient active sites were provided with the increase in Fe-RSB dosage. With the catalyst rose to 0.7 g•L^{-1}, the removal was increased by only 5%. This suggested that an increase in the catalyst dosage did not activate the oxidant to generate more radicals, likely because of the limited PAA concentration [41]. Thus, it was inferred that the Fe-RSB dosage directly influenced the concentration of the active species. At the same time, research has found that excessive use of the catalyst not only leads to the waste of materials but also reduces the removal owing to the aggregation effect [42]. Thus, Fe-RSB of 0.55 g•L^{-1} was used as the optimal concentration for following studies.

3.3.2 Influence of PAA concentration

The oxidant concentration is a crucial factor that affects pollutant removal. Thus, it was necessary to examine the effect of PAA on IMI removal (**Error! Reference source not found.**c). The removal of IMI increased from 15.4% to 81.6% as the PAA concentration increased from 0 mM to 0.25 mM. As the concentration rose to 0.5 mM, the removal efficiency of IMI decreased to 62.1%. The results showed that the PAA concentration directly affected the concentration of reactive substances. Suitable oxidant concentrations can generate numerous active species that

facilitate IMI degradation. In contrast, the use of an excessive oxidant not only resulted in waste but also quenched reactive species [43]. Thus, PAA of 0.25 mM was used as the optimal concentration for subsequent studies.

3.3.3 Influence of pH

The effect of pH on IMI degradation was also investigated (**Error! Reference source not found.**d). The results indicated that the removal of IMI decreased as the pH increased, and the removal efficiency decreased from 85.5% (pH=3) to 72.5% (pH=11). pH had a certain impact on IMI removal, and acidic conditions were found to be more effective (Figure S2). pH affected the degradation of IMI, possibly for the following reasons. Firstly, pH could affect the existence form of PAA (PAA/PAA−) [39,44]. When the solution pH exceeded the pKa of PAA (pH_pzc = 8.2), a higher pH value favored a greater proportion of PAA−. The surface of Fe-RSB was negatively charged at pHIEP > 8.75 (see supplementary materials). Furthermore, IMI existed as neutral ions within 1.56< pH_pzc <11.12 [45]. These results indicated that electrostatic interactions were not the main reason for IMI degradation by the Fe-RSB/PAA system. Second, pH could affect the leaching and hydrolysis of iron. Research has found that acidic conditions can lead to a greater leaching of iron [46]. Moreover, PAA can rapidly self-decompose and

be consumed by H_2O_2 and acetate ions under alkaline conditions (Eqs.6-8). Meanwhile, the Fe loaded on the Fe-RSB can form un-reactive iron hydroxide complexes, thereby inhibiting the catalytic efficiency [47,48]. Overall, the removal of IMI was affected by pH, primarily due to pH interference with PAA self-decomposition and iron leaching.

$$CH_3C(O)OOH + H_2O \xrightarrow{OH^-} CH_3C(O)O^- + H_3O^+ \quad (6)$$

$$CH_3C(O)OO^- + CH_3C(O)OOH \rightarrow CH_3C(O)OH + CH_3C(O)O^- + O_2 \quad (7)$$

$$CH_3C(O)OO^- + H_2O_2 \rightarrow CH_3C(O)O^- + H_2O + O_2 \quad (8)$$

3.4 Reaction mechanism

3.4.1 Insight into active radicals

Research confirmed that radicals were key to the removal of organic pollutants (e.g., $^1O_2$, •OH and R−O•) [49]. Thus, it was necessary to examine the active radicals. The presence of active substances was detected using EPR (Figure S3). The 10 mM TEMP, DIPPMO, and DMPO were used as spin trapping agents to detect the effects of $^1O_2$, •OH, $CH_3C(O)O$• and $CH_3C(O)OO$• on the removal of IMI, respectively. When Fe-RSB and PAA were mixed, the signals of •OH, $CH_3C(O)O$• and $CH_3C(O)OO$• were found (**Error! Reference**

source not found.a-b). The presence of •OH was likely attributed to the reaction between H_2O_2 and Fe-RSB in the PAA systems [50]. Nevertheless, the signals of •OH and R−O• did not appear in the PAA systems (see supplementary materials). A comparison of the PAA and Fe-RSB/PAA systems (**Error! Reference source not found.**c), the TEMP adduct signal was not observed for PAA alone, whereas there was an obvious $^1O_2$ signal in the Fe-RSB/PAA process (see supplementary materials). In summary, $^1O_2$, •OH, $CH_3C(O)O$• and $CH_3C(O)OO$• were produced after a series of complex reactions (Eqs. 9-12). The production of these active radicals led to IMI degradation.

TBA, 2, 4-hexadiene (2, 4-HD) and L-histidine reagents were used for the quenching experiments to investigate the contribution of the main active radicals to IMI degradation (**Error! Reference source not found.**d). TBA only significantly inhibits •OH [51]. 2,4-HD is frequently used to inhibit R–O• [52]. L-histidine is used as a quencher for $^1O_2$ [6]. When TBA and L-histidine was added separately to the Fe-RSB/PAA system, the removal of IMI decreased to 57.0% and 70.7%, respectively. The IMI removal was only 22.5% when 2,4-HD was added to the Fe-RSB/PAA system. Therefore, it could be inferred that $^1O_2$, •OH, $CH_3C(O)O$• and $CH_3C(O)OO$• collaborated on the removal of IMI. However, the inhibitory effect of 2,4-HD was higher than other quenching agents, which indicated that the main reactive

radicals were $CH_3C(O)O•$ and $CH_3C(O)OO•$.

$$CH_3C(O)OOH \xrightarrow{energy} CH_3C(O)O• + •OH \quad (9)$$

$$CH_3C(O)OOH + •OH \rightarrow CH_3C(O)OO• + H_2O \quad (10)$$

$$CH_3C(O)OOH + CH_3C(O)O• \rightarrow CH_3C(O)OO• + CH_3C(O)OH \quad (11)$$

$$CH_3C(O)OOH + CH_3C(O)OO^- \rightarrow CH_3C(O)OH + CH_3C(O)O^- + {}^1O_2 \quad (12)$$

3.4.2 Insight into catalytic mechanism

XPS analysis can provide insights into the valence changes of Fe during the reaction process, thereby revealing the degradation mechanisms of IMI in the Fe-RSB/PAA process. (**Error! Reference source not found.**d). Before the reaction, the binding energies (BEs) of Fe^{2+} in the Fe 2p3/2 and Fe 2p1/2 regions were 710.99 and 724.32 eV, and the BEs of Fe^{3+} were distributed to 714.97 and 729.13 eV. After the reaction, the BEs at 711.46 and 724.75 eV were Fe^{2+}, and the BEs at 715.43 and 729.80 eV were Fe^{3+}. The overall binding energies shifted to the right, and the binding energy of Fe 2p decreased. By calculating the elemental contents of the peaks before and after the reaction, the percentage of Fe^{2+} increased from 50.64% to 53.67%, whereas that of Fe^{3+} decreased from 49.36% to 46.33%.

The increase in Fe^{2+} and decrease in Fe^{3+} suggested an interconversion between Fe^{2+} and Fe^{3+}. Therefore, the change in iron valence not only triggered a series of redox reactions but also expanded the pathways to which active species were generated.

Based on the above conclusions, **Error! Reference source not found.** shows the degradation mechanism of IMI. The Fe-RSB would rapidly activate PAA, primarily generating active species like $^1O_2$, ·OH, $CH_3C(O)O·$, and $CH_3C(O)OO·$. Therefore, iron ions were considered crucial sites for the formation of active radicals. The electron transfer capacity of the biochar was enhanced by the change in the chemical states of iron. Thus, more free radicals were produced through redox reactions (Eqs. (3)-(6)). Additionally, study had found that the catalytic performance was influenced by oxygenated functional group (−OH, C=O, C−O, and Fe−O) [53]. PAA was an electron acceptor, and electron transfer led to the rupture of the functional groups in PAA, thereby generating active species. Furthermore, a large amount of $^1O_2$ was generated during the reaction. Research has shown that the –OH functional group provides an electron pathway for the formation of $^1O_2$ (Eqs. (12)) [54].

3.5 Degradation pathways and toxicity analysis of IMI

To explore the potential removal modes of IMI, UPLC-ESI-MS/MS was employed to monitor the byproducts generated during

the removal of IMI. Three routes were used to explain the degradation process (Figure S4, Figure S5). In Pathway 1, the nitroamide group on the imidazole ring was broken, and the carbon atom at the break was hydroxylated or oxidized by $^1O_2$ to form a carbonyl group (P1). The chlorine atom on the pyridine ring was then removed to obtain P2. Finally, a break in the pyridine ring near the methylene bridge occurred, followed by the formation of a carbonyl group (P3). In Pathway 2, IMI underwent dehydrogenation to form hydroxyl and carbonyl groups (P4). The carbonyl group of the nitro group in P4 broke to yield P5. Subsequently, the remaining parts of the imidazole ring fractured, forming P6. In Pathway 3, the carbon atom on the imidazole ring was hydroxylated or oxidized to produce P7. Subsequently, the nitroamide and carbonyl groups were broken to form P8. After a series of reactions, two carbonyl groups appeared on the imidazole ring to form P9. Subsequently, the n-dealkylation reaction that occurred in P9 produced P10. The intermediates were further degraded until they were fully mineralized and converted into small molecules.

ECOSAR software was utilized to estimate the toxicity of IMI and its by-products on aquatic organisms (fish, Daphnia, and green algae), and the toxicity results were shown in **Error! Reference source not found.**. In the acute toxicity front, P1, P2, P3, and P8

were toxic to green algae, whereas P10 was harmful to Daphnia and green algae. The remaining products did not harm aquatic plants, and their toxicity was significantly lower than that of IMI. In the chronic toxicity front, more than half of the intermediates showed lower toxicity than IMI. Methylpyridine and its derivatives or species with carbonyl groups formed on the imidazole ring were the most sensitive by-products. The results suggested that many products showed lower toxicity; however, further work should be conducted to reduce the toxicity of individual harmful products. Overall, the Fe-RSB/PAA process efficiently degraded IMI and caused minimal harm to the ecological environment.

3.6 Influence of HA, Cl^- and HCO_3^- on the IMI degradation

Error! Reference source not found.a shows the influence of HA on IMI degradation. As the HA concentration gradually increased, IMI degradation was inhibited (from 81.6% to 60.8%). Research has shown that HA could rapidly quench R−O•, and the reaction rate constant could reach 104 L $mg^{-1}s^{-1}$ [55]. Simultaneously, PAA and HA competed for the active sites, thereby reducing the number of free radicals generated by PAA [56].

As shown in Fig. 6b, the presence of 2 mM Cl^- slightly inhibited IMI degradation, which can be attributed to the scavenging of reactive radicals by Cl^- (Eqs. 13–14). [41]. However, when the Cl^-

concentration was increased to 10 mM, a promotional effect was observed, likely due to the generation of reactive chlorine species (RCS) that also contribute to IMI oxidation.

Error! Reference source not found.c shows the influence of HCO_3^- on the removal of IMI. The studies had indicated that the pH affected the concentration and the form of HCO_3^- [57,58]. When pH = 6.37, HCO_3^- was the predominant species in the system. Therefore, a pH of 7.0 was maintained during the reaction. The IMI removal declined from 81.6% to 59.8%. The results demonstrated that HCO_3^- inhibited the degradation of IMI. Prior study had found that HCO_3^- did not inhibit the production of R−O• in the pyrite/PAA process [39]. But HCO_3^- could react with ·OH (Eqs. (15) and (16)) [59]. Another reason could be the production of unreactive Fe-HCO_3^- complexes, thereby inhibiting the removal of PAA [41]. In this case, the inhibition of IMI by HCO_3^- was mainly due to the production of unreactive Fe-HCO_3^- complexes and the consumption of •OH.

$$Cl^- + CH_3C(O)OO\bullet + H^+ \rightarrow Cl\bullet + CH_3C(O)OOH \quad (13)$$

$$Cl^- + \bullet OH \rightarrow HClO^{-\cdot} \quad (14)$$

$$HCO_3^- + \bullet OH \rightarrow CO_3^{\bullet -} + H_2O \quad (15)$$

$CO_3^{2-} + \bullet OH \rightarrow CO_3^{\bullet -} + OH^-$ (16)

The Fe-RSB/PAA system achieved 81.6% IMI removal within 60 min using 0.55 g/L catalyst and 0.25 mM PAA at neutral pH, demonstrating performance comparable to or better than previously reported methods (Table S5). Compared to nZVI-based persulfate systems that required higher oxidant concentrations (2–10 mM), our system achieved efficient degradation with relatively low reagent consumption. Unlike photocatalytic systems that need external energy input and longer reaction times, our system operates under mild conditions without energy consumption. Furthermore, while adsorption-based biochar methods merely transfer pollutants, our system achieves complete oxidative degradation. This superior performance is attributed to (1) uniform dispersion of iron species; (2) synergy between iron sites and oxygen-containing functional groups; and (3) efficient generation of $CH_3C(O)O\bullet$ and $CH_3C(O)OO\bullet$ radicals.

3.7 Reusability of catalyst

Reusability is important in practical applications. Therefore, five cycles of Fe-RSB were performed to test the removal of IMI and reusability of Fe-RSB. The results indicated that the IMI removal declined from 81.6% to 61.9% after five cycles (**Error! Reference**

source not found.d). Although the degradation efficiency decreased, IMI was still effectively removed. Overall, Fe-RSB exhibited excellent reusability.

4. Conclusions

In this study, a relatively novel Fe-RSB catalyst was successfully synthesized via a simple pyrolysis method and employed to activate PAA for efficient IMI removal. The Fe-RSB/PAA system exhibited superior degradation performance compared to control systems, achieving 81.6% IMI removal within 60 min under optimal conditions (0.55 g/L Fe-RSB, 0.25 mM PAA, pH 7.0). Notably, the system maintained high efficiency across a wide pH range (3–11), demonstrating its robustness for treating wastewaters with varying pH conditions. Mechanistic studies revealed that $CH_3C(O)O\cdot$ and $CH_3C(O)OO\cdot$ were the dominant reactive species, alongside contributions from $^1O_2$ and ·OH, with XPS analysis confirming the crucial role of Fe^{3+}/Fe^{2+} redox cycling in PAA activation. The IMI degradation pathway involved dehydrogenation, hydroxylation/oxidation, and heterocyclic ring cleavage, with ECOSAR toxicity assessment confirming that most intermediates posed lower ecological risks than IMI. The system showed good stability and reusability, maintaining 61.9% removal after five cycles. Furthermore, the system exhibited strong resistance to interference

from HA and HCO_3^-, while high Cl^- concentrations even enhanced IMI degradation, highlighting its adaptability to complex water matrices. Overall, this work provides a promising and relatively novel approach for the remediation of IMI-contaminated water using the Fe-RSB/PAA system, highlighting its potential for practical wastewater treatment applications. While this study provides comprehensive evidence for the structural features, catalytic stability, and Fe^{3+}/Fe^{2+} redox cycling of Fe-RSB, several aspects remain unexplored, including the carbon graphitization degree, iron oxide crystalline phases, leached iron concentration, performance in real water matrices, and dynamic electron transfer behavior. Future work integrating Raman, TEM, and XRD analyses with systematic iron leaching measurement, real water matrix testing (including TOC removal), and electrochemical characterization (LSV, i-t) would further elucidate the structure-activity relationship and confirm the environmental safety and practical applicability of this system in PAA activation.

CRediT authorship contribution statement

Jinjin He: Investigation, Formal analysis, Data curation, Writing – original draft. **Baoyan Wang**: Writing – review & editing**.** **Hongwei Sun**: Writing – review & editing. **Yucan Liu**: Writing – review & editing. **Gang Wang**: Writing – review & editing. **Xiaoyong Yang**: Writing – review & editing. **Yanxiang Zhang**: Supervision, Project administration, Funding acquisition, Writing – review & editing.

Declaration of Competing Interest

The authors declare that they have no known competing financial interests or personal relationships that could have appeared to influence the work reported in this paper.

Funding

This work is financially supported by the Natural Science Foundation of Shandong Province (ZR2022QE138).

Appendix A. Supplementary data

Supplementary figures and tables are shown in the supplementary data.

References

1 Sablas, M. M. *et al.* Catalytic fluidized-bed oxidation by Fe–Mn biochar and sodium percarbonate for treating imidacloprid-contaminated water. *Chemical Engineering Journal* **521**, 166574,

https://doi.org/10.1016/j.cej.2025.166574 (2025).

2 Ji, X. *et al.* Efficiency and mechanism of adsorption for imidacloprid removal from water by Fe-Mg co-modified water hyacinth-based biochar: Batch adsorption, fixed-bed adsorption, and DFT calculation. *Separation and Purification Technology* **330**, 125235, https://doi.org/10.1016/j.seppur.2023.125235 (2024).

3 Ma, Y. *et al.* An efficient, green and sustainable potassium hydroxide activated magnetic corn cob biochar for imidacloprid removal. *Chemosphere* **291**, 132707, https://doi.org/10.1016/j.chemosphere.2021.132707 (2022).

4 Bourgin, M., Violleau, F., Debrauwer, L. & Albet, J. Ozonation of imidacloprid in aqueous solutions: Reaction monitoring and identification of degradation products. *Journal of Hazardous Materials* **190**, 60-68, https://doi.org/10.1016/j.jhazmat.2011.02.065 (2011).

5 Zhang, Q. *et al.* A novel magnetic Fe3C@Fe3O4 core–shell biochar nanocomposite derived from Zanthoxylum bungeanum pruned branches for efficient adsorption of imidacloprid. *Journal of Analytical and Applied Pyrolysis* **194**, 107544, https://doi.org/10.1016/j.jaap.2025.107544 (2026).

6 Wang, X. *et al.* Activation of persulfate-based advanced oxidation processes by 1T-MoS2 for the degradation of imidacloprid: Performance and mechanism. *Chemical Engineering Journal* **451**, 138575, https://doi.org/10.1016/j.cej.2022.138575 (2023).

7 Hladik, M. L. & Kolpin, D. W. First national-scale reconnaissance of neonicotinoid insecticides in streams across the USA. *Environmental Chemistry* **13**, 12-20, https://doi.org/10.1071/EN15061 (2016).

8 Chen, Y. *et al.* Resolution of the Ongoing Challenge of Estimating Nonpoint Source Neonicotinoid Pollution in the Yangtze River Basin Using a Modified Mass Balance Approach. *Environmental Science & Technology* **53**, 2539-2548, https://doi.org/10.1021/acs.est.8b06096 (2019).

9 Dong, X. *et al.* Interlayer-expanded LDH@biochar nanoreactors via sodium citrate mediation: Unlocking hidden active sites for persulfate-driven imidacloprid removal. *Environmental Chemistry and Ecotoxicology* **7**, 1130-1141, https://doi.org/10.1016/j.enceco.2025.05.012 (2025).

10 Su, Y. *et al.* Intestinal microbiota and metabolomics reveal the intestinal damage caused by imidacloprid in loaches (Misgurnus anguillicaudatus). *Aquatic Toxicology* **287**, 107533, https://doi.org/10.1016/j.aquatox.2025.107533 (2025).

11 Liu, J. *et al.* Exploring the role of semi-crystalline carbon nitride as exciton transition accelerator in enhancing energy transfer during photodegradation of imidacloprid. *Separation and Purification Technology* **384**, 136232, https://doi.org/10.1016/j.seppur.2025.136232 (2026).

12 Ahmed, H. R., Ealias, A. M. & George, G. Advanced oxidation processes for the removal of antidepressants from wastewater: a comprehensive review. *RSC Advances* **15**, 48639-48665, https://doi.org/10.1039/d5ra07764h

(2025).

13 Saravanan, A. *et al.* A detailed review on advanced oxidation process in treatment of wastewater: Mechanism, challenges and future outlook. *Chemosphere* **308**, 136524, https://doi.org/10.1016/j.chemosphere.2022.136524 (2022).

14 Shah, R. *et al.* Pharmaceuticals and personal care products: sources, occurrences, toxicities, and degradation by advanced oxidation and reduction processes- a review. *Separation and Purification Technology*, 135850, https://doi.org/10.1016/j.seppur.2025.135850 (2025).

15 Xia, L. *et al.* Biochar-mediated electron transfer in a spinel ferrite catalyst boosts peracetic acid activation for water decontamination. *Chemical Engineering Journal* **525**, 170068, https://doi.org/10.1016/j.cej.2025.170068 (2025).

16 Kim, J. & Huang, C.-H. Reactivity of Peracetic Acid with Organic Compounds: A Critical Review. *ACS ES&T Water* **1**, 15-33, https://doi.org/10.1021/acsestwater.0c00029 (2021).

17 Bux, N. *et al.* Catalytic degradation of organic pollutants in aqueous systems: A comprehensive review of peroxyacetic acid-based advanced oxidation processes. *Journal of Environmental Management* **373**, 123989, https://doi.org/10.1016/j.jenvman.2024.123989 (2025).

18 Zhao, W. *et al.* Unraveling the multiple role of UV in PAA/Fe(III) advanced oxidation: Mechanism, efficiency, and toxicity analysis. *Process Safety and*

Environmental Protection **194**, 1-13, https://doi.org/10.1016/j.psep.2024.12.006 (2025).

19 Panda, D., Sethu, V. & Manickam, S. Removal of hexabromocyclododecane using ultrasound-based advanced oxidation process: Kinetics, pathways and influencing factors. *Environmental Technology & Innovation* **17**, 100605, https://doi.org/10.1016/j.eti.2020.100605 (2020).

20 Kim, J. *et al.* Cobalt/Peracetic Acid: Advanced Oxidation of Aromatic Organic Compounds by Acetylperoxyl Radicals. *Environmental Science & Technology* **54**, 5268-5278, https://doi.org/10.1021/acs.est.0c00356 (2020).

21 Cai, M., Sun, P., Zhang, L. & Huang, C.-H. UV/Peracetic Acid for Degradation of Pharmaceuticals and Reactive Species Evaluation. *Environmental Science & Technology* **51**, 14217-14224, https://doi.org/10.1021/acs.est.7b04694 (2017).

22 Gaber, M. M., Toghan, A., Shokry, H. & Samy, M. Efficient oxidative degradation of organic pollutants in real industrial effluents using a green-synthesized magnetite supported on biochar catalyst. *RSC Advances* **15**, 31522-31538, https://doi.org/10.1039/d5ra04070a (2025).

23 Khan, N., Khan, M. U., Shadab, M., Siddiqui, M. B. & Siddiqui, Z. N. Polyaniline-functionalized biochar (PANI@ALB) as a heterogeneous acid–base bifunctional catalyst for one-pot cascade reactions under green reaction conditions. *RSC Sustainability* **3**, 4794-4810, https://doi.org/10.1039/d5su00279f (2025).

24 Li, M. *et al.* Biochar supported metal cobalt activated PAA to efficiently degrade CBZ: The important role of Co (IV) in the generation of peroxyacyl radicals. *Journal of Water Process Engineering* **75**, 108039, https://doi.org/10.1016/j.jwpe.2025.108039 (2025).

25 Shi, C. *et al.* Fe-biochar as a safe and efficient catalyst to activate peracetic acid for the removal of the acid orange dye from water. *Chemosphere* **307**, 135686, https://doi.org/10.1016/j.chemosphere.2022.135686 (2022).

26 Zeng, C. *et al.* Ball milling enhanced magnetic corn straw biochar for peroxyacetic acid activation towards efficient degradation of sulfadiazine. *Industrial Crops and Products* **204**, 117346, https://doi.org/10.1016/j.indcrop.2023.117346 (2023).

27 Dong, Y.-D. *et al.* Synthesis of Fe–Mn-Based Materials and Their Applications in Advanced Oxidation Processes for Wastewater Decontamination: A Review. *Industrial & Engineering Chemistry Research* **62**, 10828-10848, https://doi.org/10.1021/acs.iecr.3c01624 (2023).

28 Matos, R., Marques, I. S., Fernandes, A. J. S., Peixoto, A. F. & Fernandes, D. M. Multifunctional N,S-doped biochar decorated with transition metals as electrocatalysts for energy conversion applications. *Biomass and Bioenergy* **204**, 108463, https://doi.org/10.1016/j.biombioe.2025.108463 (2026).

29 Zeng, Y. *et al.* Nitrogen-doped carbon-based single-atom Fe catalysts: Synthesis, properties, and applications in advanced oxidation processes.

Coordination Chemistry Reviews **475**, 214874, https://doi.org/10.1016/j.ccr.2022.214874 (2023).

30 Sun, X. *et al.* Iron-modified calcium-based biochar for multi-metal stabilization in mine soil: Quantitative mechanistic insights, DFT analysis, and microbial community shifts. *Journal of Environmental Management* **395**, 127952, https://doi.org/10.1016/j.jenvman.2025.127952 (2025).

31 Kong, D. *et al.* Unveiling the mechanisms of peracetic acid activation by iron-rich sludge biochar for sulfamethoxazole degradation with wide adaptability. *Journal of Environmental Management* **347**, 119119, https://doi.org/10.1016/j.jenvman.2023.119119 (2023).

32 Yan, L. *et al.* ZnCl2 modified biochar derived from aerobic granular sludge for developed microporosity and enhanced adsorption to tetracycline. *Bioresource Technology* **297**, 122381, https://doi.org/10.1016/j.biortech.2019.122381 (2020).

33 Kiejza, D., Kotowska, U., Polińska, W. & Karpińska, J. Peracids - New oxidants in advanced oxidation processes: The use of peracetic acid, peroxymonosulfate, and persulfate salts in the removal of organic micropollutants of emerging concern − A review. *Science of The Total Environment* **790**, 148195, https://doi.org/10.1016/j.scitotenv.2021.148195 (2021).

34 He, L. *et al.* Novel insights into the mechanism of periodate activation by heterogeneous ultrasonic-enhanced sludge biochar: Relevance for efficient

degradation of levofloxacin. *Journal of Hazardous Materials* **434**, 128860, https://doi.org/10.1016/j.jhazmat.2022.128860 (2022).

35 Wu, Q. *et al.* Pyrolyzing pharmaceutical sludge to biochar as an efficient adsorbent for deep removal of fluoroquinolone antibiotics from pharmaceutical wastewater: Performance and mechanism. *Journal of Hazardous Materials* **426**, 127798, https://doi.org/10.1016/j.jhazmat.2021.127798 (2022).

36 Sun, H. *et al.* Removal Performance and Mechanism of Emerging Pollutant Chloroquine Phosphate from Water by Iron and Magnesium Co-Modified Rape Straw Biochar. *Molecules* **28**, 3290, https://doi.org/10.3390/molecules28083290 (2023).

37 Yang, C. *et al.* Ecological risk assessment and identification of the distinct microbial groups in heavy metal-polluted river sediments. *Environmental Geochemistry and Health* **45**, 1311-1329, https://doi.org/10.1007/s10653-022-01343-4 (2023).

38 Zhang, X. *et al.* Insight into the activation mechanisms of biochar by boric acid and its application for the removal of sulfamethoxazole. *Journal of Hazardous Materials* **424**, 127333, https://doi.org/10.1016/j.jhazmat.2021.127333 (2022).

39 Xing, D. *et al.* Mechanistic insights into the efficient activation of peracetic acid by pyrite for the tetracycline abatement. *Water Research* **222**, 118930, https://doi.org/10.1016/j.watres.2022.118930 (2022).

40 Carlos, T. D. *et al.* Fenton-type process using peracetic acid: Efficiency, reaction elucidations and ecotoxicity. *Journal of Hazardous Materials* **403**, 123949, https://doi.org/10.1016/j.jhazmat.2020.123949 (2021).

41 Dai, Y. *et al.* L-cysteine boosted Fe(III)-activated peracetic acid system for sulfamethoxazole degradation: Role of L-cysteine and mechanism. *Chemical Engineering Journal* **451**, 138588, https://doi.org/10.1016/j.cej.2022.138588 (2023).

42 Li, X. *et al.* Cobalt ferrite nanoparticles supported on drinking water treatment residuals: An efficient magnetic heterogeneous catalyst to activate peroxymonosulfate for the degradation of atrazine. *Chemical Engineering Journal* **367**, 208-218, https://doi.org/10.1016/j.cej.2019.02.151 (2019).

43 Dai, Y. *et al.* Enhanced degradation of sulfamethoxazole by microwave-activated peracetic acid under alkaline condition: Influencing factors and mechanism. *Separation and Purification Technology* **288**, 120716, https://doi.org/10.1016/j.seppur.2022.120716 (2022).

44 Lin, J. *et al.* Enhanced diclofenac elimination in Fe(II)/peracetic acid process by promoting Fe(III)/Fe(II) cycle with ABTS as electron shuttle. *Chemical Engineering Journal* **420**, 129692, https://doi.org/10.1016/j.cej.2021.129692 (2021).

45 Wang, G. *et al.* Characteristics of acidic hydrothermal treatment for disintegration of spiramycin fermentation residue and degradation of

residual antibiotics. *Bioresource Technology* **409**, 131234, https://doi.org/10.1016/j.biortech.2024.131234 (2024).

46 Zhang, P., Zhang, X., Zhao, X., Jing, G. & Zhou, Z. Activation of peracetic acid with zero-valent iron for tetracycline abatement: The role of Fe(II) complexation with tetracycline. *Journal of Hazardous Materials* **424**, 127653, https://doi.org/10.1016/j.jhazmat.2021.127653 (2022).

47 Zhang, L. *et al.* Activation of peracetic acid with cobalt anchored on 2D sandwich-like MXenes (Co@MXenes) for organic contaminant degradation: High efficiency and contribution of acetylperoxyl radicals. *Applied Catalysis B: Environmental* **297**, 120475, https://doi.org/10.1016/j.apcatb.2021.120475 (2021).

48 Clarizia, L., Russo, D., Di Somma, I., Marotta, R. & Andreozzi, R. Homogeneous photo-Fenton processes at near neutral pH: A review. *Applied Catalysis B: Environmental* **209**, 358-371, https://doi.org/10.1016/j.apcatb.2017.03.011 (2017).

49 Shen, W. *et al.* Activation of peracetic acid by thermally modified carbon nanotubes: Organic radicals contribution and active sites identification. *Chemical Engineering Journal* **474**, 145521, https://doi.org/10.1016/j.cej.2023.145521 (2023).

50 Tian, X. *et al.* Carbonized polyaniline-activated peracetic acid advanced oxidation process for organic removal: Efficiency and mechanisms. *Environmental Research* **219**, 115035,

https://doi.org/10.1016/j.envres.2022.115035 (2023).

51 Zhang, L. *et al.* Highly efficient activation of peracetic acid by nano-CuO for carbamazepine degradation in wastewater: The significant role of H2O2 and evidence of acetylperoxy radical contribution. *Water Research* **216**, 118322, https://doi.org/10.1016/j.watres.2022.118322 (2022).

52 Zhang, L. *et al.* Co–Mn spinel oxides trigger peracetic acid activation for ultrafast degradation of sulfonamide antibiotics: Unveiling critical role of Mn species in boosting Co activity. *Water Research* **229**, 119462, https://doi.org/10.1016/j.watres.2022.119462 (2023).

53 Zhang, Z. *et al.* Oxidation of sulfamethazine by peracetic acid activated with biochar: Reactive oxygen species contribution and toxicity change. *Environmental Pollution* **313**, 120170, https://doi.org/10.1016/j.envpol.2022.120170 (2022).

54 Wang, J. *et al.* Molybdenum disulfide (MoS2): A novel activator of peracetic acid for the degradation of sulfonamide antibiotics. *Water Research* **201**, 117291, https://doi.org/10.1016/j.watres.2021.117291 (2021).

55 Wu, W. *et al.* Degradation of organic compounds by peracetic acid activated with Co3O4: A novel advanced oxidation process and organic radical contribution. *Chemical Engineering Journal* **394**, 124938, https://doi.org/10.1016/j.cej.2020.124938 (2020).

56 Fan, G. *et al.* The dual pathway mechanisms of peroxyacetic acid activation by CoMn2O4 spinel for efficient levofloxacin degradation. *Journal of*

Environmental Chemical Engineering **11**, 109774, https://doi.org/10.1016/j.jece.2023.109774 (2023).

57 Liu, Y., He, X., Duan, X., Fu, Y. & Dionysiou, D. D. Photochemical degradation of oxytetracycline: Influence of pH and role of carbonate radical. *Chemical Engineering Journal* **276**, 113-121, https://doi.org/10.1016/j.cej.2015.04.048 (2015).

58 Wang, Z., Shi, H., Wang, S., Liu, Y. & Fu, Y. Degradation of diclofenac by Fe (II)-activated peracetic acid. Environmental Technology 42, 4333-4341, https://doi.org/10.1080/09593330.2020.1756926 (2021).

59 Wang, J. & Wang, S. Effect of inorganic anions on the performance of advanced oxidation processes for degradation of organic contaminants. *Chemical Engineering Journal* **411**, 128392, https://doi.org/10.1016/j.cej.2020.128392 (2021).

Figure and table captions

Fig. 1. The SEM images of (a) RSB, (b) Fe-RSB and (c) Fe-RSB used, (d) Nitrogen adsorption–desorption isotherms, (e) Pore size distribution, and (f) FTIR.

Fig. 2. (a) XPS survey of different biochars, XPS spectra of (a)O 1s, (b)C 1s, and (c)Fe 2p.

Fig. 3. (a) Effect of (b) Fe-RSB dose, (c) PAA and (d) pH on the removal of IMI in the PAA/Fe-RSB system. Conditions: [IMI] = 10 mg•L^{-1}, [PAA] = [H_2O_2] = 0.25 mM, [RSB] = [Fe-RSB] = 0.55 g•L^{-1}, pH = 7.0, temperature 25 ± 2 ℃.

Fig. 4. EPR spectra of (a) DIPPMO-•OH and DIPPMO-CH_3COO•, (b) DMPO-$CH_3C(O)OO$•, (c) TEMP-$^1O_2$, and (d) quenching effects of TBA, 2,4-HD and L-Histidine in the PAA/Fe-RSB system. Conditions: [IMI] = 10 mg•L^{-1}, [PAA] = 0.25 mM, [Fe-RSB] = 0.55 g•L^{-1}, [PAA: scavengers] =1:200, pH = 7.0, temperature 25 ± 2 ℃.

Fig. 5. The removal of IMI in the PAA/Fe-RSB system.

Fig. 6. Effects of (a) HA, (b) Cl^-, and (c) HCO_3^- on the removal of IMI in the PAA/Fe-RSB system, and the reusability of Fe-RSB (d). Conditions: [IMI] = 10 mg•L^{-1}, [PAA] = 0.25 mM, [Fe-RSB] = 0.55 g•L^{-1}, pH = 7.0, temperature 25 ± 2 ℃.

Table 1. Predicted acute and chronic toxicity of intermediates in the Fe-RSB/PAA system by ECOSAR.

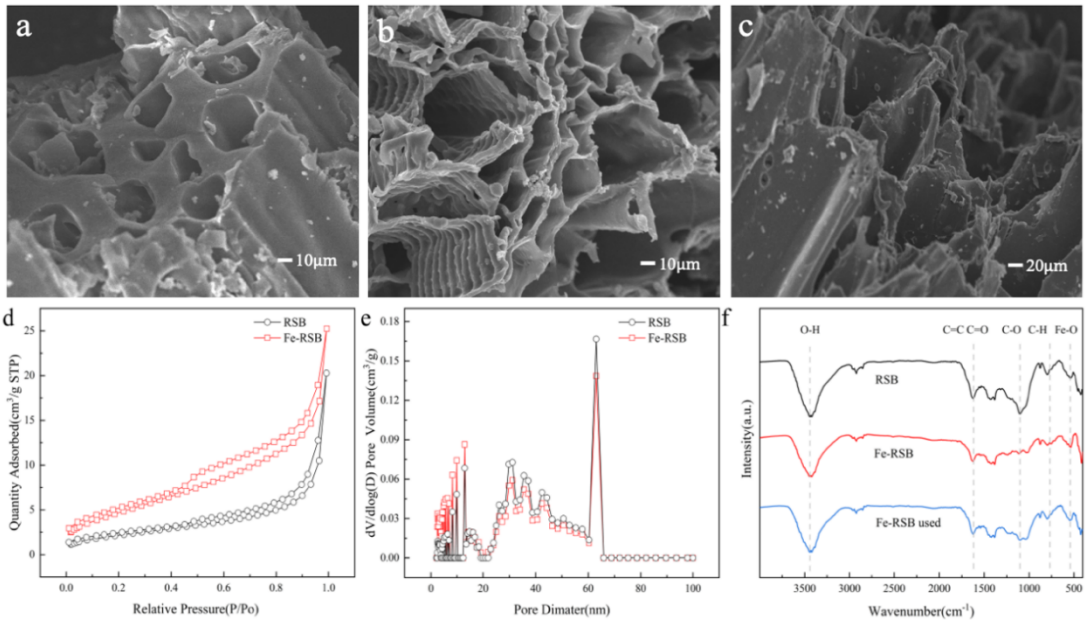

Fig. 7. The SEM images of (a) RSB, (b) Fe-RSB and (c) Fe-RSB used, (d) Nitrogen adsorption–desorption isotherms, (e) Pore size distribution, and (f) FTIR.

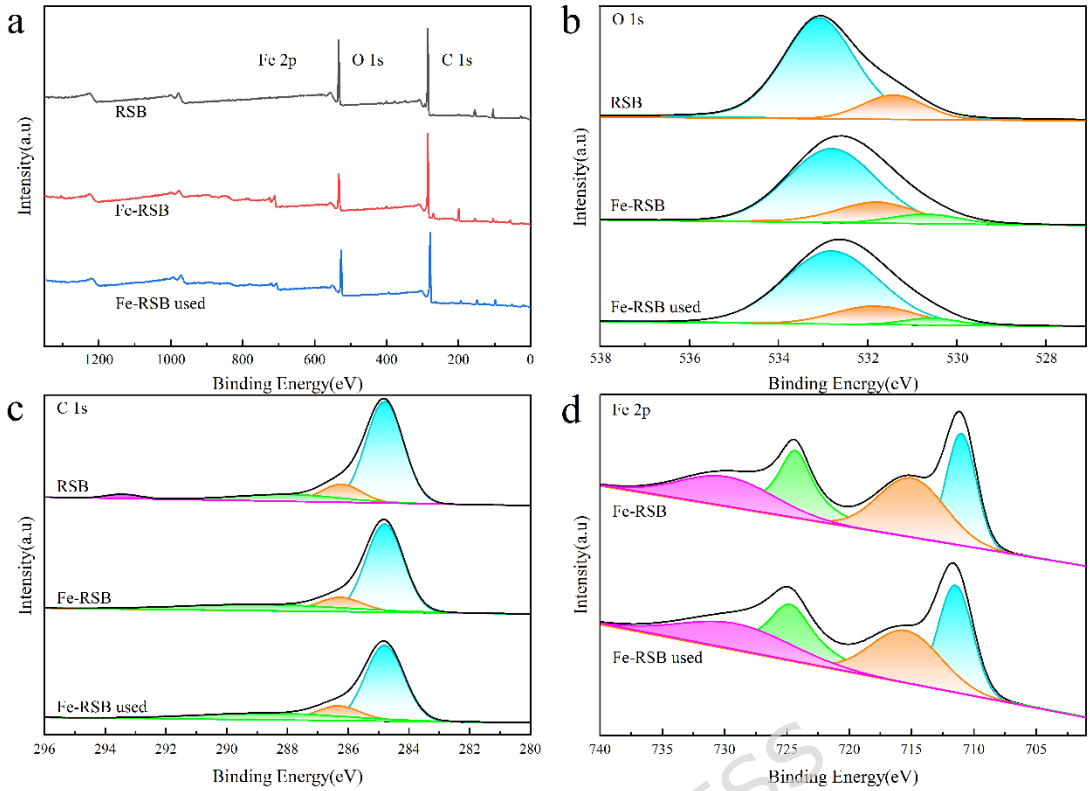

Fig. 8. (a) XPS survey of different biochars, XPS spectra of (a)O 1s, (b)C 1s, and (c)Fe 2p.

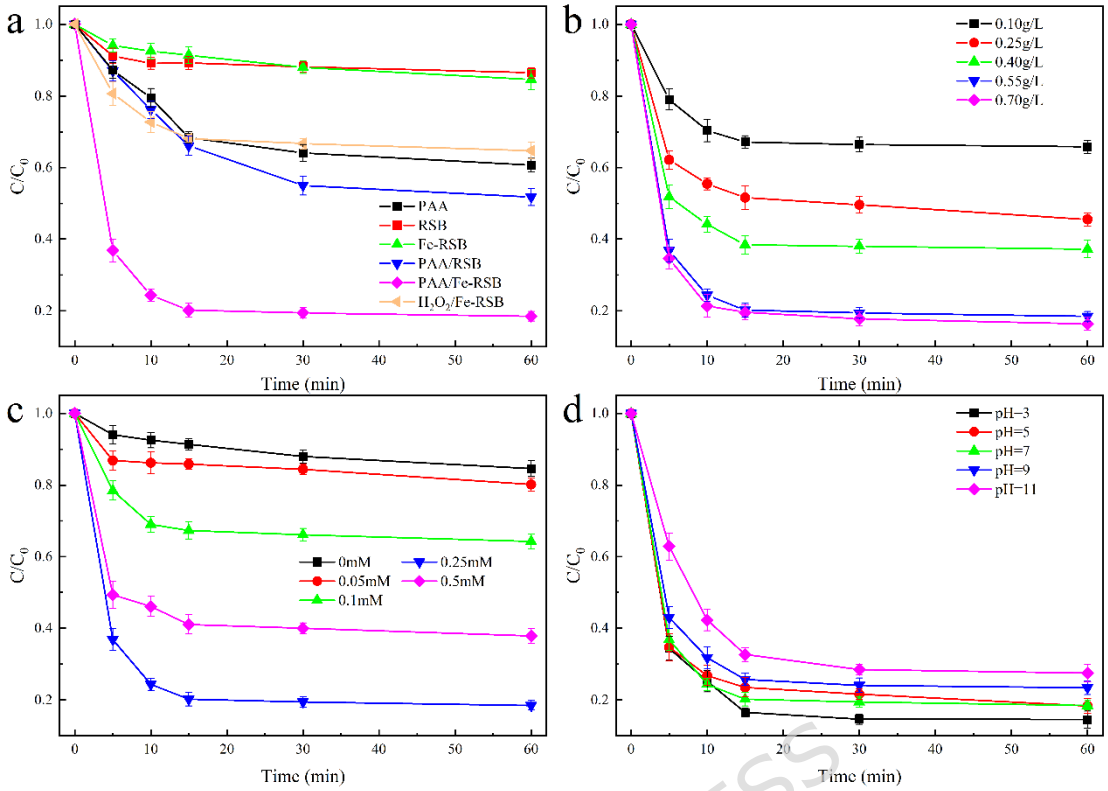

Fig. 9. (a) Effect of (b) Fe-RSB dose, (c) PAA and (d) pH on the removal of IMI in the PAA/Fe-RSB system. Conditions: [IMI] = 10 mg•L^{-1}, [PAA] = [H_2O_2] = 0.25 mM, [RSB] = [Fe-RSB] = 0.55 g•L^{-1}, pH = 7.0, temperature 25 ± 2 ℃.

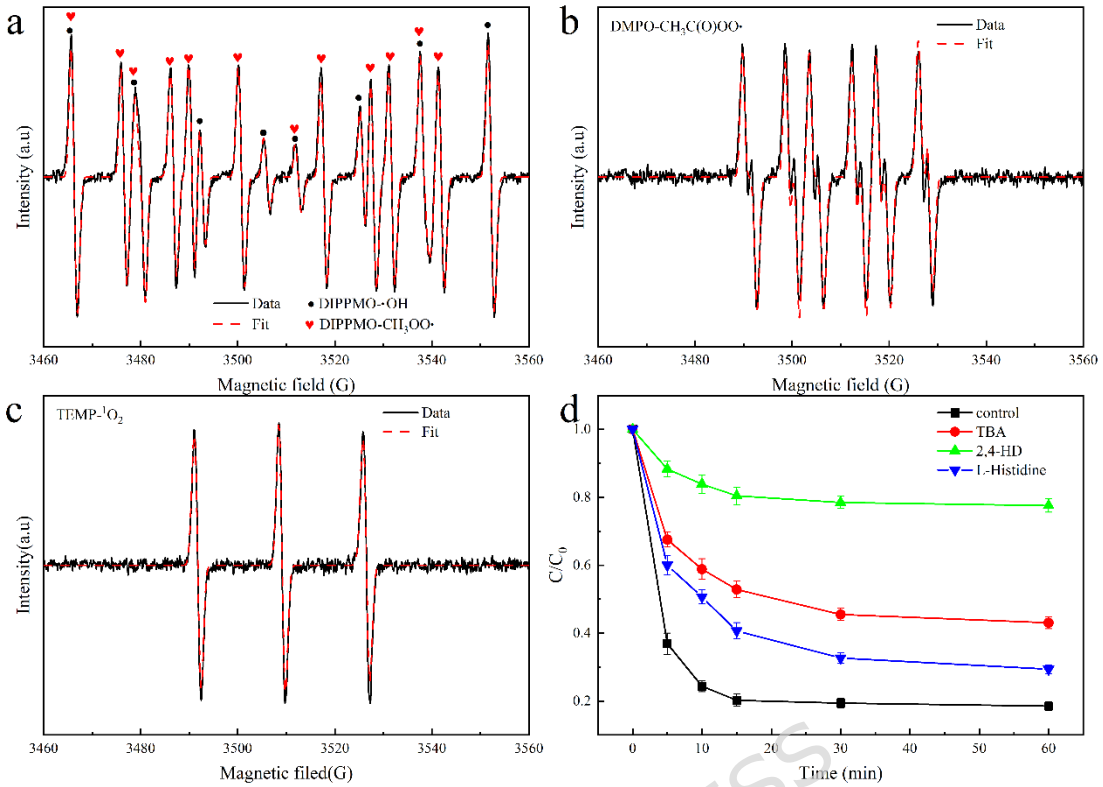

Fig. 10. EPR spectra of (a) DIPPMO-•OH and DIPPMO-CH_3COO•, (b) DMPO-$CH_3C(O)OO$•, (c) TEMP-$^1O_2$, and (d) quenching effects of TBA, 2,4-HD and L-Histidine in the PAA/Fe-RSB system. Conditions: [IMI] = 10 mg•L^{-1}, [PAA] = 0.25 mM, [Fe-RSB] = 0.55 g•L^{-1}, [PAA: scavengers] =1:200, pH = 7.0, temperature 25 ± 2℃.

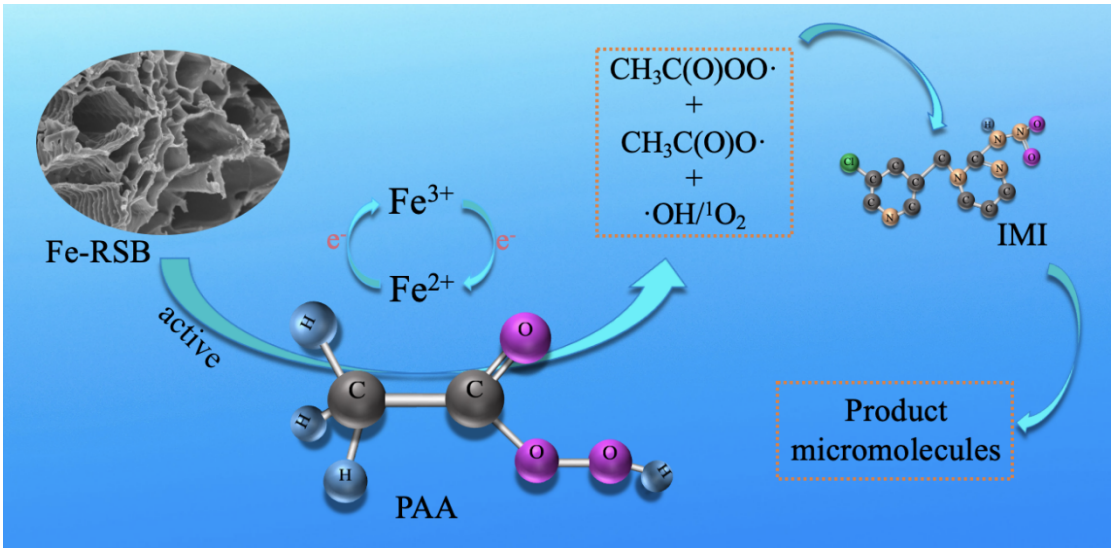

Fig. 11. The removal of IMI in the PAA/Fe-RSB system.

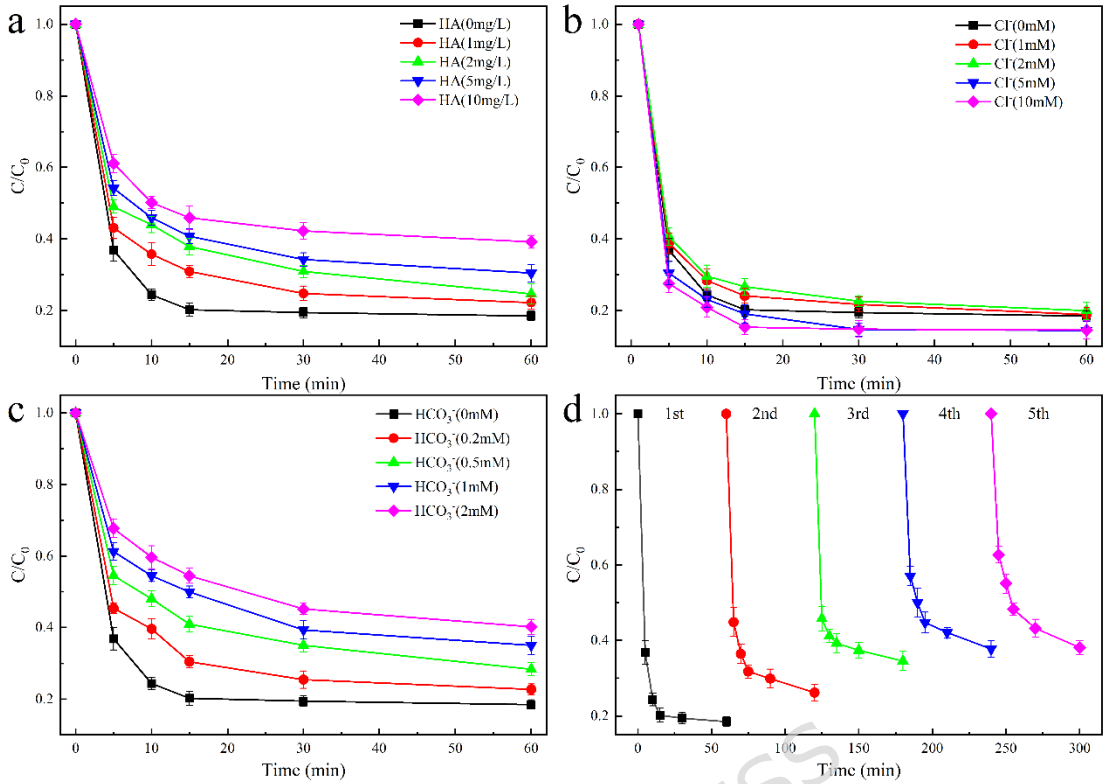

Fig. 12. Effects of (a) HA, (b) Cl^{-}, and (c) HCO_3^{-} on the removal of IMI in the PAA/Fe-RSB system, and the reusability of Fe-RSB (d). Conditions: [IMI] = 10 mg•L^{-1}, [PAA] = 0.25 mM, [Fe-RSB] = 0.55 g•L^{-1}, pH = 7.0, temperature 25 ± 2 ℃.

Table 1. Predicted acute and chronic toxicity of intermediates in the Fe-RSB/PAA system by ECOSAR.

	Acute toxicity (mg•L^{-1})			Chronic toxicity (mg•L^{-1})		
compound	Fish (96h LC50)	Daphnid (48h LC50)	Green algae (96h EC50)	Fish ChV	Daphnid ChV	Green algae ChV
IMI	436.753	44.989	50.658	42.456	3.072	14.899
P1-212	788.762	483.120	1.062	12.379	17.720	0.387
P2-177	2248.224	1702.597	1.642	30.936	46.026	0.524
P3-114	571.391	3031.977	0.009	4.132	20.257	0.002
P4-285	12680.943	994.850	1877.966	2642.216	54.413	461.131
P5-214	7622.969	608.173	1119.599	1509.045	33.812	276.006
P6-143	856.282	665.128	150.317	55.349	69.535	51.393
P7-269	1168.534	109.584	145.211	141.100	7.132	40.563
P8-225	267.691	452.528	0.017	1.928	7.447	0.005
P9-197	1179.280	107.950	150.181	153.552	6.860	41.214
P10-142	436.940	42.098	52.925	48.672	2.812	15.070

Notes: Red represents very toxic, orange represents toxic, blue represents harmful, green represents harmless.